

New insights into correlated materials in the time domain—combining far-infrared excitation with x-ray probes at cryogenic temperatures

Roman Mankowsky^{1,*}, Mathias Sander¹, Serhane Zerdane²,
Jakub Vonka¹, Marek Bartkowiak¹, Yunpei Deng¹, Rafael Winkler³,
Flavio Giorgianni¹, Guy Matmon¹, Simon Gerber¹, Paul Beaud¹ and
Henrik Till Lemke¹

¹ Paul Scherrer Institute, Villigen, Switzerland

² European Synchrotron Radiation Facility, Grenoble, France

³ Eidgenössische Technische Hochschule Zürich, Zürich, Switzerland

E-mail: roman.mankowsky@psi.ch

Received 31 January 2021, revised 16 April 2021

Accepted for publication 2 June 2021

Published 9 July 2021



Abstract

Modern techniques for the investigation of correlated materials in the time domain combine selective excitation in the THz frequency range with selective probing of coupled structural, electronic and magnetic degrees of freedom using x-ray scattering techniques. Cryogenic sample temperatures are commonly required to prevent thermal occupation of the low energy modes and to access relevant material ground states. Here, we present a chamber optimized for high-field THz excitation and (resonant) x-ray diffraction at sample temperatures between 5 and 500 K. Directly connected to the beamline vacuum and featuring both a Beryllium window and an in-vacuum detector, the chamber covers the full (2–12.7) keV energy range of the femtosecond x-ray pulses available at the Bernina endstation of the SwissFEL free electron laser. Successful commissioning experiments made use of the energy tunability to selectively track the dynamics of the structural, magnetic and orbital order of Ca_2RuO_4 and $\text{Tb}_2\text{Ti}_2\text{O}_7$ at the Ru (2.96 keV) and Tb (7.55 keV) *L*-edges, respectively. THz field amplitudes up to 1.12 MV cm^{-1} peak field were demonstrated and used to excite the samples at temperatures as low as 5 K.

Keywords: free electron laser, strongly correlated materials, ultrafast, resonant x-ray diffraction, THz excitation, instrumentation, cryogenic

(Some figures may appear in colour only in the online journal)

1. Introduction

One fundamental goal of condensed matter science is to understand and manipulate materials with functionalities that are

relevant for technological applications such as high temperature superconductivity, giant magnetoresistance and insulator-to-metal transitions [1, 2]. The ground state a material attains under given external conditions depends on the strong interaction between magnetic, electronic and structural degrees of freedom, giving rise to complex energy potentials with multiple local minima corresponding to phases with very different macroscopic properties. Traditionally, this subtle interplay between the various degrees of freedom is explored by

* Author to whom any correspondence should be addressed.

Original content from this work may be used under the terms of the [Creative Commons Attribution 4.0 licence](https://creativecommons.org/licenses/by/4.0/). Any further distribution of this work must maintain attribution to the author(s) and the title of the work, journal citation and DOI.

controlling the sample environment, e.g. temperature and pressure, or by applying chemical doping and large electric and magnetic fields, thereby favoring one phase against another. Because of the central role atomic and electronic order plays in these materials, angle-resolved photoemission spectroscopy, neutron as well as x-ray scattering techniques have become essential tools to determine and study the rich phase diagrams of correlated materials [2–5], complementing measurement of macroscopic physical quantities.

Commonly, these studies are performed in the adiabatic limit, restricting direct quantitative information on the relevance of individual parameters and their coupling strength. Ultrafast spectroscopies circumvent these limitations by applying the principle of causality: the response of the system to an ultrafast perturbation of selected degrees of freedom is measured on their inherent timescales. With energy values of a few eV down to meV for electronic excitations and collective phenomena, respectively, the relevant timescales in solids range from fs to ps.

The field of ultrafast phenomena is governed by tabletop lasers, providing ultrashort optical pulses used to repetitively excite the material and sample its response with a second laser pulse with varying temporal delay in a stroboscopic manner. In solid systems dynamics related to coherent atomic motion [6–8], quasiparticle dynamics [9, 10], changes of the electronic configuration [11] and phase transitions [12–15] can be observed. But optical probes are in many cases not sufficient to unambiguously identify and quantify the underlying correlations. In the past decades, more direct and quantitative probes have been developed to overcome these limitations, including time- and angle-resolved photoelectron spectroscopy [16–18] and scattering techniques employing ultrashort electron [19–22] or x-ray pulses [23] with femtosecond time resolution. In crystalline systems, time-resolved x-ray diffraction (tr-XRD) provides quantitative information about coherent transient changes of the atomic lattice. Away from elemental absorption edges, x-rays interact predominantly with tightly bound core level electrons, providing information about the relative positions of atoms with sub-pm precision. Pioneering work has been conducted over decades with low-count photon sources, investigating coherent lattice motions and structural phase transitions [24–33].

1.1. Time-resolved x-ray diffraction at FELs

The development of free electron lasers (FEL) delivering high-brightness femtosecond pulses with wavelengths at the Ångström range [34–38], allows performing time resolved XRD studies with unprecedented precision [39–47]. In particular the prospects of tuning the x-ray photon energy offers application of more selective but also more photon hungry x-ray techniques tailored to investigate complex materials with femtosecond temporal resolution. For reviews on material studies performed at FELs, see for example references [48, 49].

Namely, time-resolved resonant x-ray diffraction (tr-RXRD) combines the atomic resolution of XRD with the element specific sensitivity of x-ray absorption spectroscopy

(XAS) to probe electronic configurations by tuning the x-ray energy to an electronic transition and fulfilling the Bragg condition. tr-RXRD has been used to selectively follow the dynamics of order in the electronic system uncovering interaction between the spins, charges, orbitals and the atomic lattice [50–54]. XRD and RXRD are essentially measuring material properties close to the center of the Brillouin zone with small momentum transfer and, in some cases, also commensurate or incommensurate modulations of atomic lattice and/or electronic order. Since the momentum of hard x-rays covers multiple Brillouin zones, access to the changes in the dispersion of modes and their fluctuations, an elementary ingredient in many phase transitions, is in principle also possible. Taking advantage of the high brilliance of the x-ray pulses offered by FEL's, time-resolved experiments have indeed been pushed to the inelastic regime by applying resonant inelastic x-ray scattering [55] to retrieve changes in magnetic fluctuations from the simultaneous measurement of the momentum and energy transfer of collective excitations [51, 56]. The energy resolution of these experiments has been limited to around 100 meV from a trade-off with photon counts.

Lower energy modes up to around 5 THz (20 meV) can be investigated by analyzing the momentum-dependent frequencies of coherently excited modes in the diffuse x-ray scattering around and between Bragg peaks in the time domain, yielding for example the acoustic phonon dispersions [57] or as recently shown elucidate the dynamics of local lattice distortions [58]. For example, by employing diffuse x-ray scattering it could be shown that the photoinduced insulator-to-metal transition of vanadium dioxide is of order–disorder type, rather than occurring through a coherent displacive mechanism [59]. The ultrafast change in the lattice potential unlocks the vanadium atoms and yields large-amplitude uncorrelated motion.

1.2. Selective excitation

Photo-excitation of electronic transitions in the 1–3 eV range deposits locally a significant amount of energy. The various relaxation mechanisms from this strong perturbation of the electronic states result in a complex chain of events which are often difficult to disentangle [60]. These considerations triggered strong interest of the community in more tailored pump sources in the far infrared wavelength range (10–1000 μm) to coherently drive low energy excitations (1–100 meV) such as coherent lattice modes [39, 61, 62] or control of the magnetic subsystem [54, 63, 64]. In particular, it has been shown that coherent excitation of lattice modes can induce insulator–metal transitions [65, 66], switch the electric polarization [15] or even enhance superconductivity [39, 62]. These experiments, however, become more complex as they demand (in addition to the control of the sample temperature) large focusing optics very close to the sample to reach the MV cm^{-1} electric field strengths required to drive changes and reveal higher order coupling effects, which appear as a nonlinear response [46, 61, 63, 67]. Combining resonant low-energy excitation with the newly developed selective FEL techniques described above will be key in disentangling the coupling between the various degrees of freedom in correlated

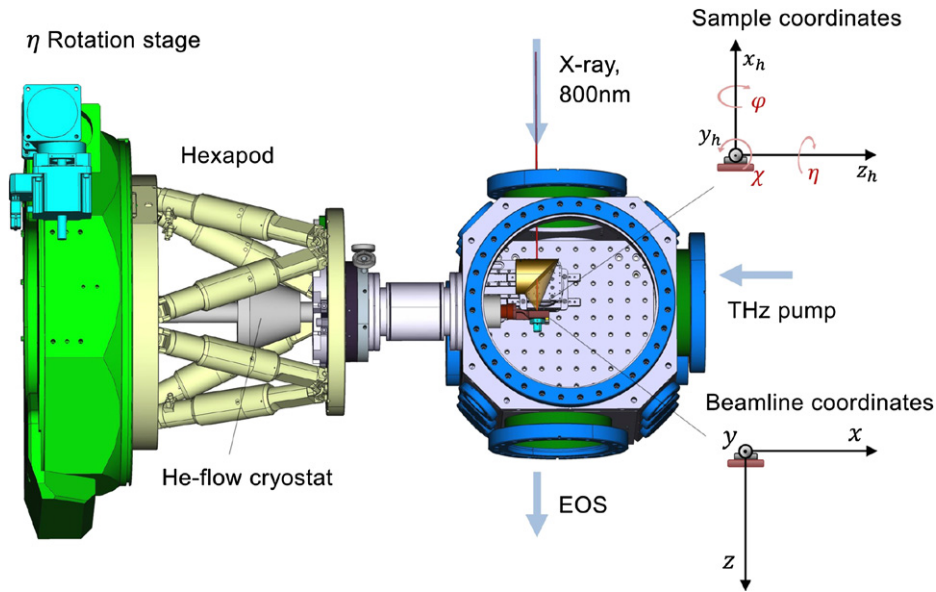


Figure 1. Sketch of the experimental geometry and the sample chamber as seen from top. The laser pump pulses enter through an exchangeable window on the right side of the chamber and are focused onto the sample with a parabolic mirror. The x-ray pulses are pass through a hole in the parabolic mirror and diffracted upwards from the sample. The 800 nm pulses used for characterization of the THz field by electro-optic sampling (EOS) take the same path as the x-rays and can exit through the downstream window of the chamber.

materials and in developing techniques to control their functional properties on ultrafast timescales for future devices.

1.3. Sample environment

In order to access relevant phases of materials and prevent thermal excitations from obscuring the induced effects, experiments need to be performed at low sample temperatures [68, 69]. We report here the concept and performance of a new design of a cryogenic vacuum chamber for (resonant) XRD experiments at sample temperatures down to 5 K, permitting high-field excitation from the ultraviolet to the far infrared. The design remains compatible with the large x-ray photon energy range of 2–12.7 keV available at the Bernina endstation [70] of SwissFEL [38], which offers element specificity covering absorption edges ranging from *M* (Dy to U), *L* (Rb to Tl) and *K* (P to Se). Successful commissioning experiments were performed on melting of magnetic and orbital order in Ca_2RuO_4 and excitation of a hybrid mode in $\text{Tb}_2\text{Ti}_2\text{O}_7$.

2. Instrumentation

2.1. Design concept

To prevent condensation at the sample surface at cryogenic temperatures, working in a vacuum environment is inevitable, which additionally facilitates experiments at low energy x-rays down to 2 keV. The experimental chamber design developed here is depicted in figure 1 along with major components, which include sample cooling, sample motion and main light propagation paths. The sample is mounted on the cold finger of a helium flow cryostat, which is motorized outside vacuum by a 6 degree of freedom hexapod (coordinate system x_h, y_h, z_h), mounted to a large rotation stage used for the main

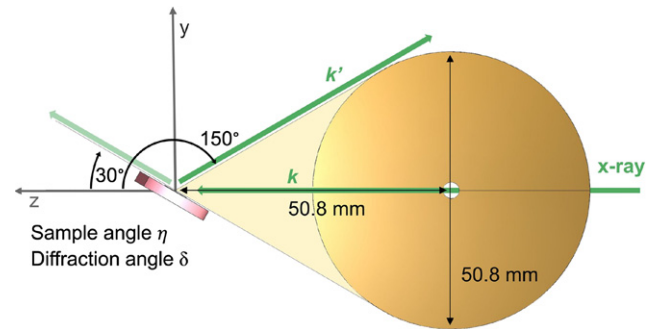


Figure 2. Detailed view in negative x -direction on the sample, as well as the parabolic mirror with 50.8 mm diameter and focal distance. The sample rotation η around the z_h -axis and the elevation of diffracted x-ray pulses k' within the y - z plane are limited to $(30\text{--}150)^\circ$.

sample rotation η around the z_h -axis. All sample orientation and diffraction angles are defined according to a frequently used convention (You [71]), except for ν , which was replaced with γ to prevent mix-ups during the beamline control due to similarities between the detector and sample motions ν (nu) and μ (mu).

In order to reach high THz excitation fields at the sample, the chamber was designed around the laser focusing optics, which consists of a 2' diameter, 2' focal distance gold-coated parabolic mirror, with five motorized motion degrees of freedom in vacuum. The size of the parabolic mirror restricts both the range of the x-ray incidence angle as well as the diffraction angles as sketched in figure 2: the rotation of the sample around the z_h -axis is limited to $\eta = (30\text{--}150)^\circ$. Beyond this range, the sample clips the cone of THz light focused by the parabolic mirror. In analogy, the directions of the diffracted x-ray beam k' from the sample surface are limited in elevation

Table 1. Ranges of accessible values of δ for scattering within the z - y plane (forward/backward) and the x - y plane (sideways). Given are the optimal δ values, taking the geometrical limitations by the THz focusing optics into account, as well as the accessible angles with the Beryllium window and the in-vacuum detector. γ denotes the azimuth rotation of the diffracted x-ray beam around the y axis away from the direct beam.

Scat. plane	Optimal	Be window	In-vacuum
z - y ($\gamma = 0$)	$(30\text{--}150)^\circ$	$(38\text{--}141)^\circ$	$(34\text{--}146)^\circ$
x - y ($\gamma = 90$)	$(0\text{--}90)^\circ$	$(18\text{--}117)^\circ$	$(19\text{--}127)^\circ$

angle $\delta = (30\text{--}150)^\circ$ by the sample surface and the parabola for forward or backward scattering in the y - z plane, respectively. In contrast, diffraction sideways in the x - y plane away from the hexapod is not obstructed significantly. Furthermore, diffraction to the left and right side of the x-ray beam (view from above) is identical for centrosymmetric samples. An ideal x-ray window would therefore allow for an elevation range of $\delta = (0\text{--}90)^\circ$ of the photons scattered sideways in the x - y plane away from the hexapod.

The accessible solid angle for diffracted x-rays is maximized by placing the sample vertically as close as possible to the large diameter CF250 top flange, onto which either a Beryllium window or an in-vacuum detector can be mounted. The large flange also allows a design, which lowers the window or detector further into the chamber, reducing the vertical distance to the sample down to 36 mm. Additionally, the sample position is offset towards the hexapod with respect to the center of the top flange in order to optimize the accessible solid angle for diffraction to the side (x -direction). Table 1 summarizes the optimal situation, as well as the accessible δ values for the two detection options on the top flange.

Investigation of high-quality single crystal samples by means of x-ray diffraction requires a precise and reproducible adjustment of the sample angles with respect to the incident x-rays. To meet this requirement within the tight space constrained by the laser focusing optics, the sample motorization is installed outside vacuum. It makes use of the large, high-resolution rotation stage shown in green in figure 1 onto which a heavy load hexapod for fine positioning is mounted. The motions are transferred into vacuum by a differentially pumped rotation stage and a bellows designed to be compatible with the torque applied when rotating the sample around the z_h axis in η . Table 2 summarizes the range and precision of the available motorized motions.

With this sample positioning concept, sample holders can directly be fixed to the cold finger of the cryostat, ensuring high thermal conductivity and therefore optimal cooling efficiency. This is crucial because the bulky focusing optics require a large solid angle at the front side of the sample to be free of thermal heat shielding, which would block the THz radiation. In addition to adjusting the incidence angle to the surface, THz pump experiments often require the option to rotate the sample around its surface normal to align the crystal axis with respect to the THz polarization vector and to access additional diffraction peaks. This motion is realized by combining a 360°

Table 2. Range and specified stage precision of the available sample motions for the THz and grazing incidence (GI) sample holders. See figures 1 and 4 for the definition of the translation axes and angles of the THz and GI sample holders, respectively. The second 360° motion in ϕ around the sample normal for the THz sample holder is a manual rotation, facilitated by a wobble stick. For GI experiments, the rotations μ^* and χ , facilitated by the hexapod, are used to align the sample surface to the η rotation stage. The x-ray incidence angle μ is adjusted by large ry rotation stages underneath the chamber and the η stage (limited to $\sim 3^\circ$ with a precision of $2\ \mu\text{rad}$).

THz holder	GI holder	Range	Precision
x_h	x_h	12 mm	$0.1\ \mu\text{m}$
y_h	y_h	12 mm	$0.1\ \mu\text{m}$
z_h	z_h	70 mm	$0.1\ \mu\text{m}$
$rx_h(\phi)$	$rx_h(\chi)$	3°	$100\ \mu\text{rad}$
$ry_h(\phi)$	—	360°	2°
$ry_h(\chi)$	$ry_h(\mu^*)$	3°	$100\ \mu\text{rad}$
$rz_h(\eta)$	$rz_h(\eta)$	360°	$2\ \mu\text{rad}$

manual rotation of the sample using a wobble stick with a $\pm 1.5^\circ$ motorized range given by the hexapod.

Following these conceptual ideas, we designed an octagonal chamber, separated inside into two levels, with alternating CF160/CF40 and CF100/CF40 ports on the 8 sides, respectively. The two levels are separated by an aluminium breadboard with M6 threads mounted to the wall of the chamber, which supports the parabola motion stages and temporary components during the set-up phase. The cryostat port, focusing optics and the wobble stick are all placed in the upper compartment close to the CF250 top flange. The CF40 ports are used for sample viewing. The ports in the lower compartment are connected to a $355\ \text{l min}^{-1}$ turbo pump (Pfeiffer HiPace 400) as well as electric feedthroughs for the parabola motion stages and a fast diode detector measuring the coarse x-ray/laser pulse arrival times.

Exchanging samples involves opening and closing the chamber, which takes approximately 2 h including warm up, cool down and thermalization. A pressure of 5×10^{-6} mbar is typically reached within 30–45 min. The design was prioritized over a larger chamber, which could include a sample load lock to insert samples directly into vacuum, because it facilitates small distances to in-atmosphere components from the top or the side. The drawback of increased sample exchange time is mitigated by a smaller chamber volume and by the typically long measurement time on the same sample in pump/probe experiments. The foreseen installation of additional liquid nitrogen cooled shields described in section 2.4 will further increase the pump speed.

2.2. Sample holder for THz pump experiments

In addition to the motorized motions, the sample can be rotated by 360° manually around its surface normal in ϕ using a wobble stick. The mechanics are integrated into the sample holder, which consists of three components as shown in figure 3(a). The base (1) is directly screwed onto the cold finger for efficient thermal contact. It holds a Cernox thermometer and the

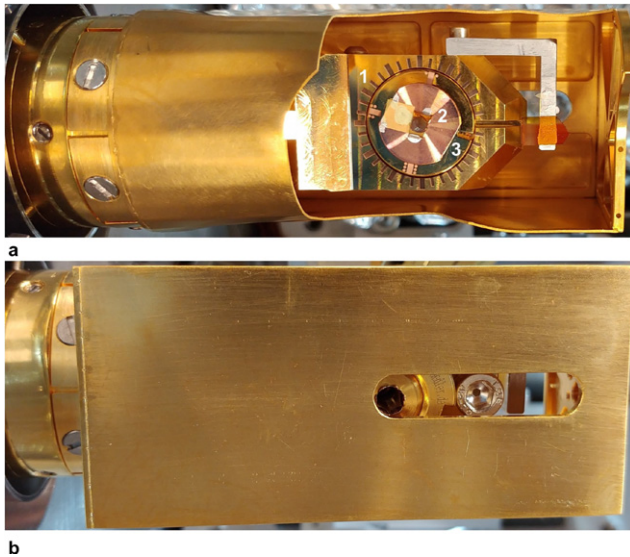


Figure 3. (a) Front side of the sample holder. 1, 2 and 3 denote the base, sample mount and rotating plate which make up the sample holder. The crystal used for electro-optic sampling is mounted onto the L-shaped angle piece. (b) Back side of the sample holder. The sample can be manually rotated around its surface normal with a wobble stick through a cut-out in the radiation shield and fastened using the screw afterwards. The shield moves together with the motorized sample translations and rotations.

crystals used for electro-optic sampling (EOS). For simple sample exchange, samples are glued onto small 15 mm diameter holders (2), which are screwed into a plate (3), which is part of the rotation mechanism and not removed during sample exchange. This plate can be rotated manually using a hex ball driver on the wobble stick from the back side as shown in figure 3(b) without need for warming up or venting the chamber. After rotation, it is pressed against the base with a screw, also actuated by the wobble stick. During operation, all three parts are firmly pressed against each other over a large area for efficient thermal contact.

2.3. Grazing incidence sample holder

The sample holder for THz excitation can be exchanged for a second design optimized for x-ray grazing incidence (GI) experiments, a geometry typically used to match the x-ray probe depth to the pump penetration depths for wavelengths ranging from the near infrared to the ultraviolet (2000 – 250) nm. Here, the incidence angle is kept fixed and the sample azimuth is adjusted to access various diffraction peaks. In GI geometry, the sample surface normal is parallel to the cold finger to make use of the high precision large η rotation-stage for this rotation as shown in figure 4. The same motorized motions as discussed above for the THz sample holder are available as given in table 1. Note that due to the different geometry, rotations around the sample coordinate system define different angles. The rotations μ and χ facilitated by the hexapod are used to align the sample surface to the η rotation stage. The x-ray incidence angle can be adjusted by a large $ry(\mu)$ rotation stage, which rotates the whole η stage together with the heavy load hexapod and the sample around the vertical beamline axis

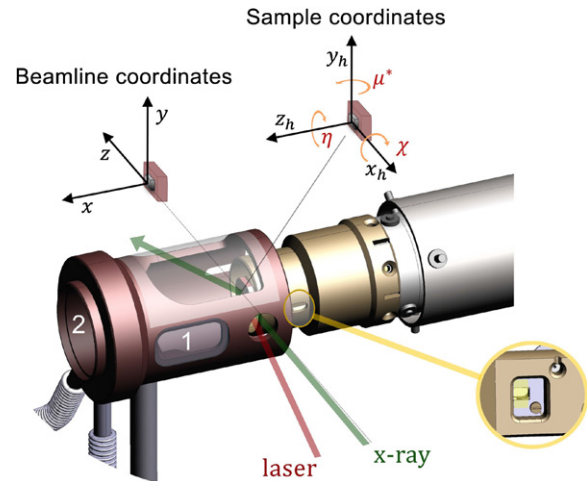


Figure 4. Grazing incidence sample holder. The sample surface normal is parallel to the cryostat coldfinger. It is shielded by a liquid nitrogen cooled fixed shield (on the left side) and a He exhaust gas cooled shield, which rotates with the sample (right side, golden). The angle between laser and x-ray pulses can be adjusted between (0–10)° and both enter through a 12 mm opening in the fixed shield. The x-rays exit through an aluminized mylar foil and Spectrosil windows (1) and (2) are used for sample viewing. Spatial and temporal overlap can be aligned using a YAG screen, which transmits the laser pulse.

with a precision of 2 μ rad. To keep the cold finger normal to the chamber wall, the chamber can be rotated around the same axis using the stages of the heavy load goniometer underneath [70]. The x-ray incidence angle is then limited to around 3° by the bellow connecting the chamber to the beamline if no window is used.

The sample is shielded by a combination of a 40 K He exhaust gas cooled shield (1), which rotates with the sample, and an 80 K liquid nitrogen cooled shield fixed to the chamber. The angle between pump laser and x-ray pulses can be adjusted between (0–10)° and both enter through a 12 mm diameter opening in the shield. The x-rays exit through a mylar foil coated with 200 nm of aluminium, which acts as a heat shield on the top side of the sample holder.

Spatial overlap can be established visually via fluorescence from a YAG screen, mounted in the same depth in beam direction z as the center of the sample holder, which can be moved into the beam by translating the sample holder further into the fixed shield along z_h . Temporal overlap is established by recording the x-ray induced absorption change of the transmitted laser beam outside the chamber. The diffraction solid angle is the same as for the THz sample holder and discussed in detail in section 2.6.

2.4. Cooling

The sample is cooled with a commercial Helium flow cryostat from CryoVac GmbH with 4 W cooling power at 4 K and a nominal temperature range from 3.5 to 500 K. Temperature control and heating is achieved with a 50 W heater mounted inside the cold finger assembly. A diode and a Cernox sensor are available for temperature measurements on the

Table 3. Calculated absorbed radiative power by the sample holder from the surrounding chamber and the parabola body without shield, with the He exhaust gas cooled shield (S1) and with the LN₂ cooled plates (S2).

Shielding	Chamber (mW)	Parabola (mW)	Total (mW)
No shields	2270	187	2457
S1	915	187	1102
S1 + S2	670	187	857

cold finger and the base of the sample holder, respectively. For experiments requiring an electronic connection of the sample, a feedthrough with 6 0.2 mm diameter Manganin wires, which are thermalized on the cold finger and on the heat exchanger, are installed. In addition, a free CF16 port is available for an optional user supplied feedthrough.

The lowest temperature that can be reached is given by the cooling power of the cryostat, which depends on the Helium flow, and the power absorbed from radiative heat sources. The main heat sources are the surrounding 300 K black body radiation of the chamber and the radiation from the body of the parabolic mirror, which are listed in table 3. As the spectra of the THz pump pulses covering 0.1 THz to 30 THz overlap with the 300 K black body radiation, shielding the front side of the sample holder is nontrivial. Solutions include spectral filtering with band pass filters or filtering by polarization using wire grid polarizers. A third option is to use a large circular plate as shield with a cut-out, which rotates synchronized at the 100 Hz repetition rate of the pulsed laser and x-ray sources. However, all of these options have disadvantages. Optical components reduce the electric field of the THz pump pulses and the rotating shield complicates sample viewing and can cause collisions.

Therefore, we focused on achieving a high cooling power by ensuring a good thermal contact of the sample with the cold finger as described in section 2.1 and shielding all areas, which do not block the laser pump pulses and the incident and diffracted x-ray probe pulses. The shield reduces the absorbed power from 2.5 W to 1.1 W. With the shield shown in figure 3 and a He consumption of 2.2 L h⁻¹ and 1.2 L h⁻¹, stable temperatures of 5 K and 7.5 K can be reached, respectively, allowing for 1.5 or 3 days of continuous operation with a 100 L liquid He Dewar. For experiments, which require low temperatures for longer periods, the Dewar can be exchanged without heating up the sample to room temperature. During this procedure, which takes around 40 min including thermal stabilization, the sample heats up to around 70 K from 5 K base temperature.

The temperature-dependent cooling power of the cryostat can be estimated by measuring the temperature reached for various heater settings. The total cooling power is given by the compensated heat sources, i.e. the sum of heater power and absorbed radiative power of 1.1 W. A linear dependence between temperature and cooling power is a good approximation down to 5 K. From the fit shown in figure 5, we extract a cooling power of 960 mW at 5 K with a He consumption of 1.3 L h⁻¹. Therefore, the absorbed radiative power of 1.1 W has to be reduced by 150 mW to reach 5 K. The planned

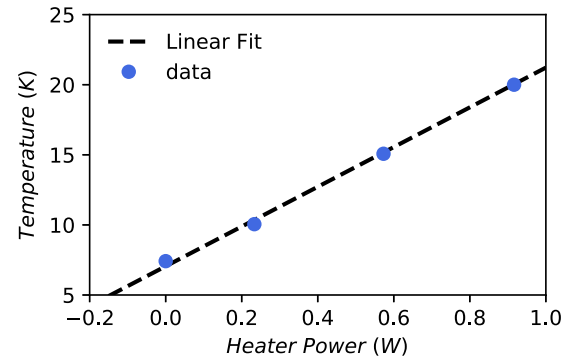


Figure 5. Temperature measured at the sample holder for different heater settings with the heat shield of figure 3 installed and 1.3 L h⁻¹ liquid helium consumption.

installation of additional liquid nitrogen cooled shielding around the chamber walls facing the sample with a high emissivity coating will reduce the heat load by 250 mW, allowing for more efficient cooling. Furthermore, the plates will act as a cold trap, speeding up the process of pumping down the chamber after sample exchange.

2.5. Pump pulse focusing and diagnostics

2.5.1. THz focusing setup. As described in section 2.1, the sample chamber was designed around the laser focusing optics, which consist of a 2' diameter, 2' focal length gold coated parabolic mirror. The mirror is motorized in vacuum with encoded piezo stages from SmarAct GmbH in x_p and z_p translations and rx_p , ry_p , rz_p rotations (see figure 6 and table 4). Here, the x_p and z_p motions are used for horizontal and vertical overlap of the THz with the x-rays, respectively. ry_p and rz_p are used to optimize the focus by aligning the parabola. Vertically, the sample is brought to the x-ray beam height by moving the whole chamber using the stages underneath.

The pump laser enters the chamber through a differentially pumped viewport with a 58 mm clear aperture exchangeable window and is guided to the parabolic mirror. The x-ray probe pulses pass through a hole in the parabolic mirror in a collinear geometry and are diffracted upwards from the sample. To measure the electric field of the pump pulses and optimize the focus, EOS is performed at the sample position. The electric field at the sample location is probed by 800 nm laser pulses. This near IR laser beam is coupled into vacuum upstream of the chamber and propagates collinearly with the x-rays, guided with the x-ray beam through the same hole in the parabola, and exits the chamber through the downstream window. The crystal used for EOS is mounted onto an L-shaped holder to the base of the sample holder (figure 3(a)) to permit field measurements during the experiment without warming up the sample and venting the chamber.

The performance of the optical setup was tested during the preparation of two experiments, which required THz pulses with central frequencies of 0.5 THz and 2.5 THz, generated by optical rectification of 7.4 mJ, 100 fs, 800 nm pulses in LiNbO₃ and 1.7 mJ, 35 fs 1.5 μ m in DSTMS, respectively. The optical imaging systems used to expand the beam to match the

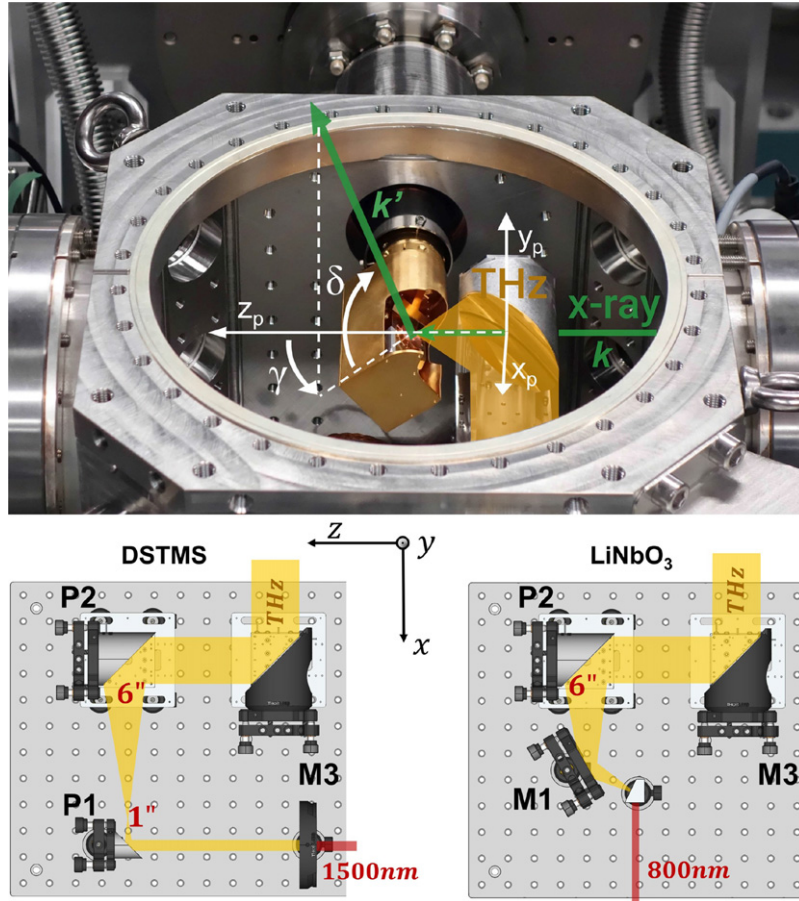


Figure 6. Upper panel: sketch of the experimental geometry and the sample chamber. The direction of the diffracted x-rays (green) is defined by the angles γ and the elevation δ . The direct beam is defined by $\gamma = \delta = 0$. The axis x_p , y_p and z_p describe the motorized motions of the parabola mirror. Lower panel: optical imaging scheme for the DSTMS and LiNbO₃ THz generation setup. M and P denote flat and parabolic gold coated mirrors.

Table 4. Range and repeatability of the available motions of the parabolic mirror. x_p , z_p and rx_p , ry_p , rz_p denote translations along and rotations around the axis shown in figure 6.

Motion	Range	Repeatability
x_p	69 mm	105 nm
z_p	41 mm	60 nm
ry_p	90°	0.26 μ rad
rx_p	10°	0.03 μ rad
ry_p	10°	0.03 μ rad

chamber parabola diameter and adjust its divergence are shown in the lower panels of figure 6. In both setups, the THz pulses are collimated with a 6' focal distance, 2' diameter parabolic mirror P2 and brought into the chamber with a flat elliptical mirror M3. Both the parabola P2 and mirror M3 are motorized in x direction and can be moved together to adjust the THz divergence. The THz focus is brought onto the sample surface in x-ray beam direction by moving the in-vacuum parabola in parallel with the incoupling mirror M3 along z . The incoupling mirror is further motorized in ry and rz to adjust the pointing onto the chamber parabola. The THz generation boxes were purged with N₂ gas up to the window of the vacuum chamber.

In both commissioning experiments, a 8 mm thick ZEONEX window from Tydex compatible with ultrahigh vacuum (UHV) was used. See figure 10 for details about its transmission in the THz range.

2.5.2. Electro-optic sampling. To characterize the THz field strength in the same conditions as the experiment under vacuum, a $\langle 110 \rangle$ oriented GaP crystal with 100 μ m thickness was mounted on the sample holder. The spectral content and field strength were characterized by EOS using copropagating 800 nm pulses, which are focused to a spot size of 85 μ m full width at half maximum (FWHM) and have a duration of 100 fs and 50 fs for the LiNbO₃ and DSTMS setup, respectively. The polarization of the THz (vertical) and 800 nm (horizontal) pulses was aligned along the $(-1, 1, 0)$ and the $(0, 0, 1)$ in-plane axes of the GaP crystal, respectively.

As the 800 nm pulses propagate through the GaP crystal, their electric field components projected onto the $(-1, 1, 1)$ and $(-1, 1, -1)$ axis experience birefringence, which is proportional to the THz electric field strength [72, 73]. The induced phase retardation between the two components Γ rotates the polarization of the 800 nm pulses. The polarization state was measured by converting the linear polarization to elliptical polarization using a $\lambda/4$

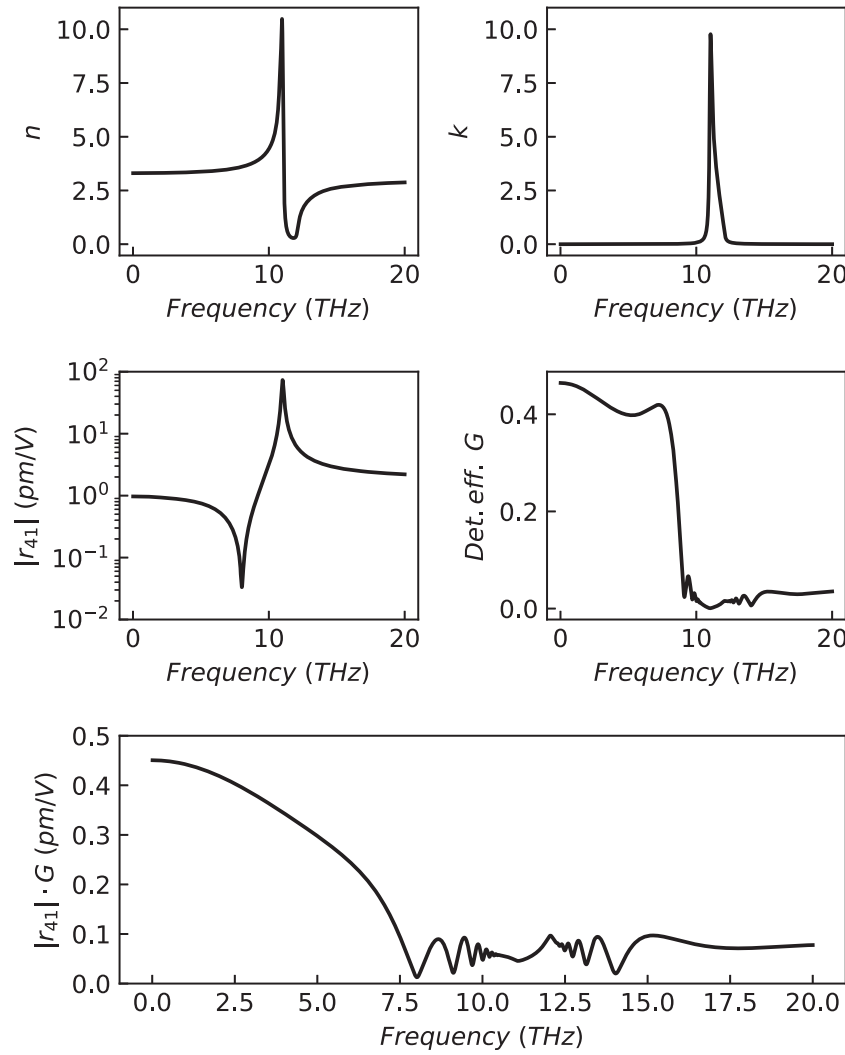


Figure 7. Calculated parameters for electro-optic sampling of THz fields in 100 μm GaP following [75]. Upper panels: real n and imaginary k part of the refractive index, showing an absorption peak due to an optical phonon at 11 THz. Middle panels: frequency-dependent electro-optic coefficient $|r_{41}|$ and detection efficiency G (see text for details). Lower panel: overall frequency dependence $|r_{41}| \cdot G$ of the electro-optic detection sensitivity.

wave plate and separating it into its horizontal and vertical components with a Wollaston prism. The intensities of the two pulses have then been recorded separately with two photodiodes (Thorlabs SM1PD1A). Without induced birefringence by the THz electric field, the $\lambda/4$ wave plate was aligned to create circular polarization from the horizontally polarized 800 nm probe pulses by balancing the intensity on the two photodiodes. The induced phase retardation can be reconstructed from the intensity measured on the two diodes I_1 and I_2 according to $\Gamma = \arcsin((I_1 - I_2)/(I_1 + I_2))$ [74]. An issue with the detection of very high THz electric fields approaching MV cm^{-1} with EOS is that the induced phase difference in the GaP crystal can exceed $\pi/2$, and higher order effects can become important, breaking the linear dependence between the polarization rotation and the electric field strength. In order to stay in the linear regime, the THz fields were attenuated to $T = 31.6\%$ (10% transmission of the intensity) using a commercial metal coated Si wafer from Tydex (see figure 10 for the measured transmission). The THz field strength can then

Table 5. Parameters of the THz generated in LiNbO₃ and DSTMS crystals with 7.4 mJ, 100 fs 800 nm and 1.7 mJ, 35 fs 1.5 μm pump pulses, respectively. Given are the THz pulse duration and spot size (both in intensity, FWHM) and peak field, measured by EOS in the focus of the chamber parabola under vacuum (see text for details).

Crystal	Pulse duration (fs)	Focus ($d_x \times d_y$) (μm^2)	E _{peak} (MV cm^{-1})
LiNbO ₃	614	442×855	0.75
DSTMS	219	184×200	1.12

be reconstructed from the phase retardation acquired by the 800 nm pulses according to formula (1) [73].

$$E(t) = \frac{\Gamma \cdot \lambda}{2\pi d n_0^3 \cdot r_{41}(\omega) \cdot G(\omega) \cdot T} \quad (1)$$

Here, λ and n_0 denote the wavelength and refractive index of the 800 nm pulses, d the thickness of the GaP crystal

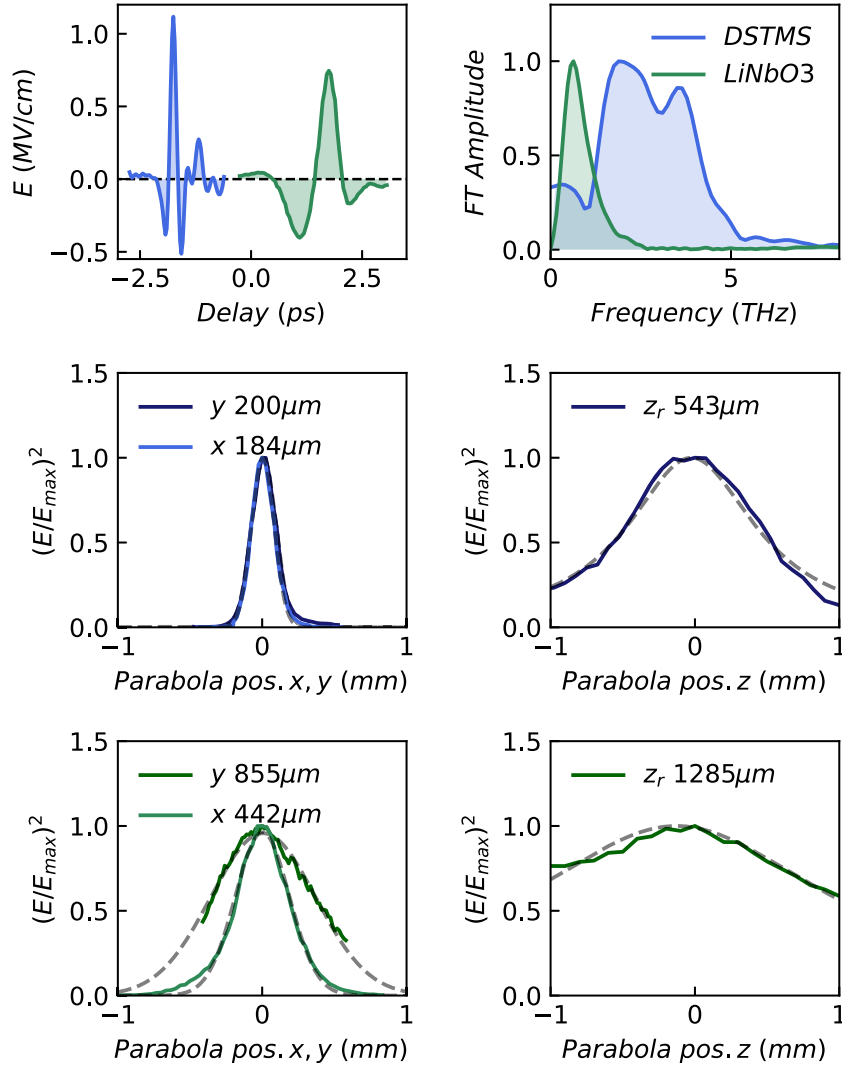


Figure 8. EOS measurements. Upper panels: electric field and spectrum of focused THz radiation inside the chamber in vacuum, generated in LiNbO₃ and DSTMS. Lower panels: planar (x_p , y_p) and depth (z_p) spatial overlap scans at the peak of the EOS trace. Shown is the intensity $I = E^2$. The given numbers are the FWHM spot sizes for the planar scans and the Rayleigh length z_r for the depth scan.

Table 6. Parameters of the THz generated in LiNbO₃ and DSTMS calculated using the measured pulse energy, spot size and pulse duration (see text for details).

Crystal	Pulse energy (μ J)	E_{peak} (MV cm ⁻¹)
LiNbO ₃	11	2.07
DSTMS	1.7	4.36

and T the transmission of the THz electric field through the attenuator. The first remaining factor $r_{41}(\omega)$ describes the electro-optic coefficient of GaP at 800 nm sampling wavelength. The second factor $G(\omega)$ describes the detection efficiency taking the Fresnel reflectivity losses of the THz pulses at the GaP surface and mismatch between THz phase velocity and the 800 nm group velocity into account. These properties are in general THz frequency ω dependent. Figure 7 shows the frequency dependence of the electro-optic coefficient and

the detection efficiency for the 100 μ m GaP crystal used here, calculated following [75]. To retrieve the quantitative value of the electro-optic coefficient $r_{41}(\omega)$, the calculation has been normalized to $|r_{41}(9.45 \text{ GHz})| = 0.88 \text{ pm V}^{-1}$ reported for 800 nm sampling pulses [76].

Absorption due to the infrared-active phonon mode at 11 THz is clearly visible in the refractive index. In addition, the electro-optic coefficient r_{41} is strongly modulated in the vicinity of the phonon mode, first reducing the magnitude, followed by a resonant enhancement at the TO frequency of the phonon mode. The detection sensitivity G shows a sharp cut-off at 8.5 THz. This cut-off can be shifted to higher frequencies with thinner GaP detection crystals [75] at the expense of a reduced overall signal according to equation (1) and the need to optically connect the crystal to an electro-optic inactive substrate to prevent Fabry–Pérot resonances from distorting the measurement [77]. The overall frequency dependence of the electro-optic detection scheme starts to fall off above 2 THz,

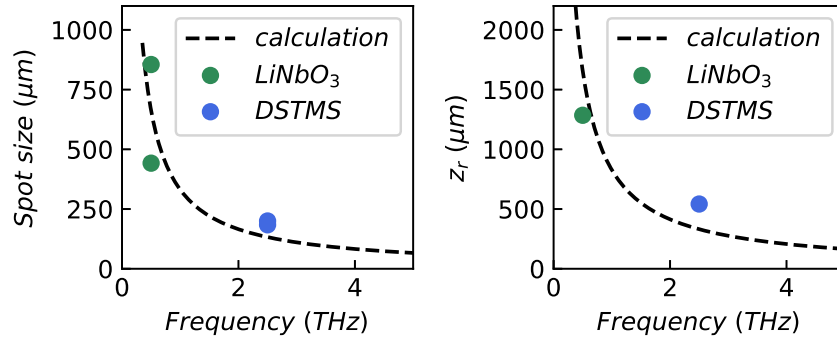


Figure 9. Calculated FWHM spot size and Rayleigh length as described in the text, assuming a parabola focal distance of 50 mm and beam waist radius of 23.5 mm before focusing. The experimental values for the beam size in x and y as well as the Rayleigh length z_r obtained from the spatial EOS overlap scans of figure 8 are shown as points.

reaching 0 at around 7.5 THz as shown in the lower panel of figure 7.

The frequency content of the THz radiation generated in the DSTMS crystal covers a range of (0–5) THz. In order to account for the frequency dependence of the detection sensitivity, the relative difference of the diode traces $(I_1 - I_2)/(I_1 + I_2)$ was corrected in the frequency domain by taking the Fourier transform and then transformed back to the time domain. For LiNbO₃, a constant value of $r_{41}(\omega) \times G(\omega) = 0.47 \text{ pm V}^{-1}$ can be used because the spectral content only covers (0–1.5) THz.

Figure 8 shows the characterization of THz pulses by EOS with 85 μm FWHM diameter 800 nm pulses under vacuum in the focus of the chamber parabola. The THz spot size and Rayleigh length were derived by scanning the THz focusing parabolic mirror in x and rx , and in parallel with the incoupling mirror M3 along the beam direction z , respectively. During the scans, the relative delay between THz and 800 nm sampling pulses was kept fixed at the maximum of the EOS trace. The THz FWHM pulse duration, spot size and peak electric field measured by EOS are given in table 5. With both setups, electric peak fields above 0.7 MV cm^{-1} were reached.

With the knowledge of the THz pulse duration and spot size, the peak field can also be calculated from its pulse energy u using formula (2), assuming a Gaussian pulse. Here, ϵ_0 and c represent the vacuum electric permittivity and the speed of light.

$$E_{\text{peak}} = \sqrt{\frac{4\sqrt{\ln 2/\pi} \cdot u}{\epsilon_0 c \cdot \tau \cdot A}} \quad (2)$$

The THz pulse energy u was measured with a commercial powermeter at the sample position and presents a lower limit as the chamber was vented and the THz radiation attenuated due to a beam path of around 300 mm in air, which was not present in the EOS measurements and the experiment. The spot size $A = \pi/4 \times d_x d_y$ and FWHM pulse duration τ are taken from the values measured by EOS reported in table 5. The results of the THz peak field are reported in table 6.

We find a clear discrepancy between the peak electric field derived from EOS and the measured pulse energy by a power meter, the latter being larger by a factor of 2.5

and 3.8 for LiNbO₃ and DSTMS, respectively. The reconstructed field strength from EOS represents a lower limit as any misalignment of the polarization of the 800 nm and THz pulses, rotation of the GaP crystal as well as averaging due to the spot size and pulse duration of the sampling pulses can reduce the detected signal. At the same time, the pulse energy recorded by the powermeter could be easily overestimated due to the small intensity, especially for DSTMS. Therefore, we report here the values derived by EOS as performance indicators.

The lower panels of figure 8 show that the focus size and length reduce significantly for increasing frequency of the THz pulses. Therefore, the motion along the beam direction (z) becomes important in the higher frequency THz range, for which the Rayleigh length of the focused beam z'_r , can be shorter than 100 μm . The dependence of the focus size and Rayleigh length on the THz frequency ν can be estimated by propagating a Gaussian beam with beam waist radius ω_0 before the parabola and representing the parabola as ideal thin lens with focal length f . Here, the beam waist ω_0 is defined as the radius, at which the intensity of the THz pulses reduced to $1/e^2$, related to its FWHM by $\omega_0 = \text{FWHM}/\sqrt{2 \cdot \ln 2}$. The beam waist ω'_0 and Rayleigh length z'_r after focusing are given by:

$$\omega'_0 = \frac{f \cdot c}{\pi \omega_0 \nu} \quad (3)$$

and

$$z'_r = \frac{f^2 \cdot c}{\pi \omega_0^2 \nu}, \quad (4)$$

where c denotes the speed of light. Therefore, both the Rayleigh length and spot size are proportional to $1/\nu$. Calculations assuming $f = 50 \text{ mm}$ and $\omega_0 = 23.5 \text{ mm}$ are shown in figure 9 together with the experimentally measured values. Note that these calculations just show the general dependencies. In order to accurately predict the spot size, a full ray tracing is required, taking the divergence of the individual spectral components of the THz pulses into account.

Due to the limited preparation time available at the FEL beamline, the reported electric fields represent a conservative tuning achievement, which is likely to be reached routinely for user beamtimes. The comparison of these results with

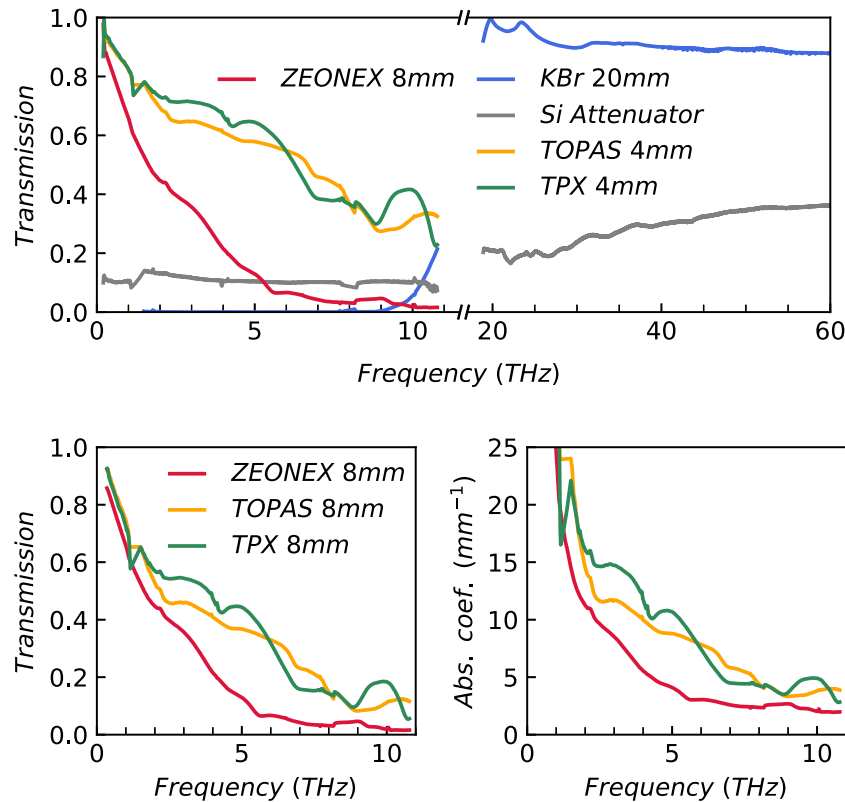


Figure 10. Upper panels: transmission of several window materials in the THz ranges accessible with DFG in LiNbO_3 and organic crystals as well as GaSe. Shown is also the measured transmission of the metalized Si attenuator from Tydex (10% transmission of the intensity), which was used to reduce the field strength for the THz pulse characterization by EOS. Lower panels: extracted absorption coefficient and calculated transmission of 8 mm thick materials. The measurements were done at the IR beamline of the Swiss Light Source [78].

values obtained in a fully optimized laboratory setup shows that at least double the field strength can be reached by an optimization of the THz generation and focusing.

2.5.3. THz window transmission. The THz electric field was additionally attenuated by the relatively thick 8 mm window made of ZEONEX, a material suitable for UHV applications. Future efforts will go into the investigation of other polymer window materials and their stability after repeated venting and pumping cycles. The frequency resolved transmission of the intensity through the 8 mm ZEONEX as well as 4 mm TPX and TOPAS is shown in the upper panel of figure 10. The lower panels of the same figure show the extracted absorption coefficients taking the Fresnel reflectivity losses into account as well as the calculated transmission for 8 mm thickness of the measured materials.

Using TPX or TOPAS as window material could not only increase the field strength but also shift the frequency cut-off due to the onset of phonon absorption to higher frequencies. Another option, which will be evaluated, is the generation of the THz field in a box evacuated to pre-vacuum of around 2×10^{-2} mbar connected to the experimental chamber. The small remaining differential pressure can be held by a thin membrane, strongly reducing absorption losses of the THz pulses at the expense of a more complicated venting and pumping procedure. Whether the (organic) crystals used for the THz generation have to be actively cooled to prevent damage at 100 Hz operation has to be investigated. All stages used for

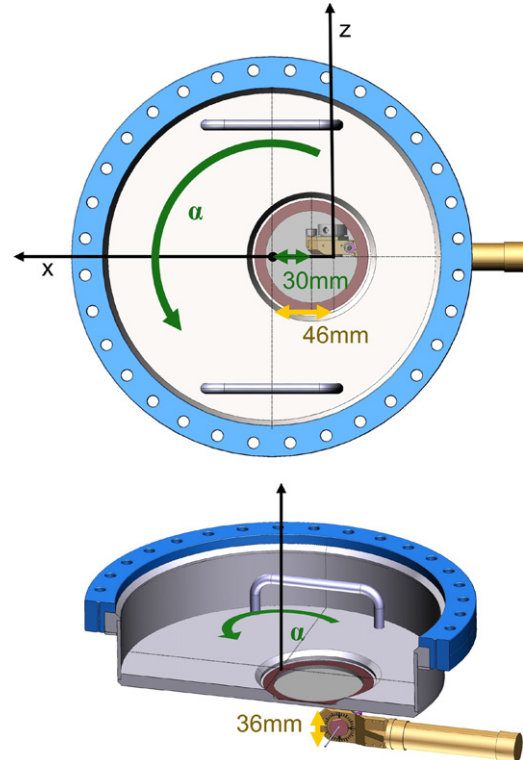


Figure 11. CF250 Beryllium window flange. The 70 mm diameter 250 μm thick Be window is offset by 30 mm in x -direction from the center of the chamber top flange. The offset of the sample 46 mm in the same direction.

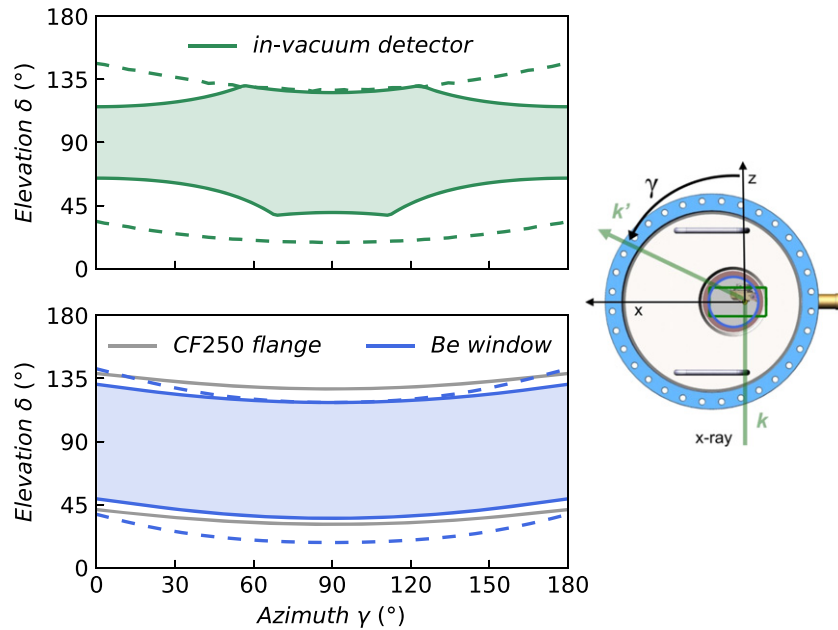


Figure 12. The filled area between the solid lines denotes the accessible combinations of δ and γ angles for the Be window (blue) and in-vacuum detector (green) positioned directly above the sample as depicted on the right side of the figure. The dashed lines denote the cumulative angles reachable when considering all possible rotations of the flanges around their center. The grey lines denote the limits at which diffracted beams are blocked by the top of the CF250 flange (blue in figure 11). δ values outside this range can only be reached by lowering a detector inside the Be window assembly.

the motorization of the THz optics are already high-vacuum compatible.

2.6. X-ray diffraction angles

The chamber has a CF250 top flange, which can accommodate various window or detector options for x-ray detection. While a Be window in combination with a detector outside the chamber is a viable option for hard x-rays (5–12.7 keV), in-vacuum detector solutions are required for the tender x-ray range (2–5 keV), or for experiments, which are very sensitive to air scattering. The following section presents two solutions already available at Bernina and briefly summarizes a third in-vacuum detector option, which is currently being designed.

The direction of the diffracted x-rays (k' , green arrow in figure 6) is defined by its azimuth rotation around the y -axis γ and the elevation δ . X-ray scattering to the right and left side along the beam direction (positive and negative γ) yields the same physical information. Therefore, the sample, parabola and x-ray entry are all offset by -46 mm along x with respect to the center of the chamber, optimizing the diffracted solid angle on one side.

2.6.1. Beryllium window. For hard x-rays, a 250 μm thick, 70 mm diameter Be transmission window is available. In order to maximize the accessible diffraction angles, it is lowered into the flange with a vertical distance of 36 mm to the sample and offset horizontally by 30 mm from the center of the flange as shown in figure 11. Therefore, the available scattering angles depend on the rotation angle α of the flange around its center.

A calculator for accessible δ and γ angles in dependence of the Be flange rotation is available on the Bernina instrument

website <https://psi.ch/en/swissfel/bernina>. The full accessible range combining all possible rotations of α (dashed) as well as the range for the Beryllium window placed centered above the sample (solid) are displayed in figure 12 in blue.

2.6.2. Fixed in-vacuum detector. For experiments which cannot tolerate any x-ray beam path through air due to absorption or scattering, an in-vacuum Jungfrau pixel detector [79] is available. Similar to the Be window assembly, the 0.5 M Jungfrau detector with $75 \times 75 \mu\text{m}$ pixel size and a total active area of $80 \times 40 \text{ mm}^2$ is fixed onto a rotatable flange with an eccentricity of 36 mm as shown in figure 13. Due to the short vertical distance of 42 mm to the sample, the detector covers a large solid angle as shown in figure 12. The angular resolution remains fixed as the sample-detector distance cannot be changed.

2.6.3. Motorized in-vacuum detector. For experiments, which require a vacuum environment and higher angular resolution, a motorized in-vacuum detector assembly is currently being designed. The concept is shown in figure 14. The 0.5 M Jungfrau detector is mounted onto a flange at higher sample distance, which is welded on a bellow allowing angular motion of the entire detector. The detector can be rotated around the center of the CF250 flange γ_{det} and its elevation angle δ_{det} can be varied. To prevent torsion of the large bellow (green) due to γ_{det} rotations, the mount of the detector can freely rotate around the central normal axis of its top face (red arrow). This free rotation is captured by an absolute encoder. As both motorized angular rotations are centered at the bottom of the flange instead of the sample, the exact δ and γ values for each detector pixel have to be

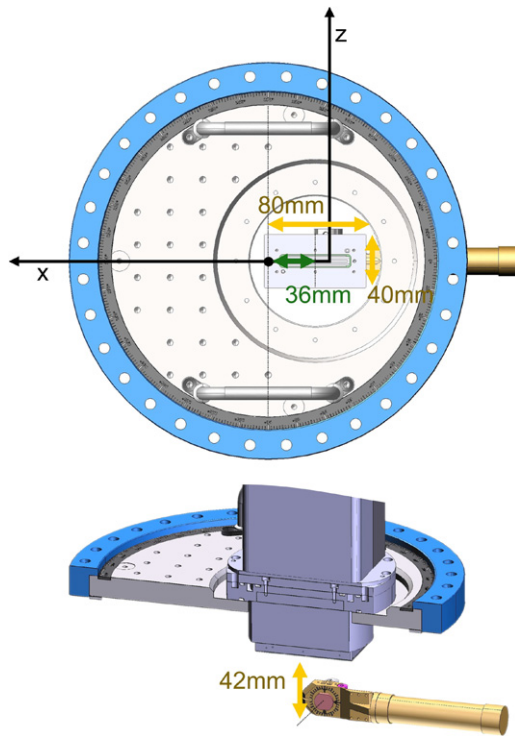


Figure 13. Fixed in-vacuum detector assembly. The detector center is offset by 36 mm in x -direction from the center of the chamber top flange. The $80 \times 40 \text{ mm}^2$ active area is lowered into the flange with a distance of 42 mm to the sample.

calculated from the encoder read-back values measuring the exact mechanical rotations. The x-rays enter the bellow through a 110 mm diameter aperture with a vertical distance of 34 mm from the sample.

The sample-detector distance is 245 mm, which can further be increased by adding additional distance pieces at the cost of reduced accessible solid angle. The angular and momentum resolution for 2 and 5 keV are given in table 7 for fixed and motorized in-vacuum detectors. Note that the resolution of the fixed detector strongly depends on the elevation angle δ , because the flat detector surface is not aligned towards the sample. The resolution (i.e. angular range covered by a detector pixel) is worst directly above the sample and best for sideways scattering at the smallest possible δ value.

3. Setup performance

The performance of the described experimental chamber has been tested by two experiments, investigating the melting of magnetic and orbital order in Ca_2RuO_4 and the excitation of a hybrid mode in $\text{Tb}_2\text{Ti}_2\text{O}_7$. The first experiment combined 15 K low temperature with resonant x-ray diffraction at the Ruthenium L-II edge (2.96 keV), making use of the in-vacuum detector to prevent strong air absorption. In the second experiment, a hybrid magnetoelastic mode was resonantly excited by THz pulses and the response of the orbital and structural order measured independently by tuning the x-ray photon energy on and off the Tb L-III edge at 7.5 keV.

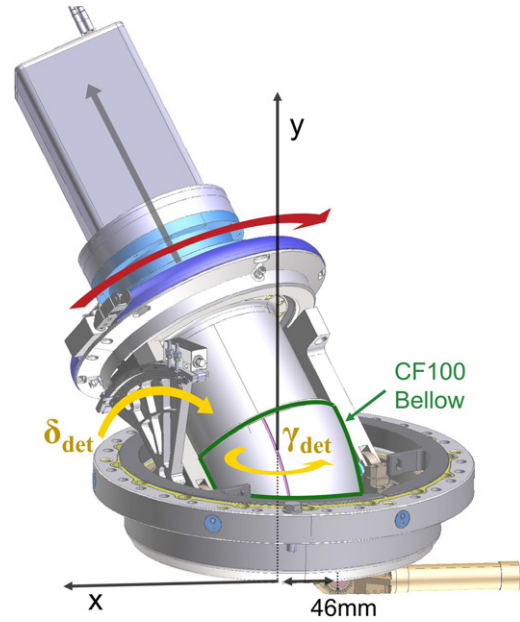


Figure 14. Concept of the motorized in-vacuum detector assembly. The distance between sample and the detector active area is 245 mm. The rotation of the detector around the center of the CF250 flange δ_{det} as well as the elevation γ_{det} are motorized to increase the accessible diffraction angles. Due to the 46 mm offset of the sample along the x -axis, these angles are different from δ and γ defined in figure 6. To prevent torsion of the large bellow (green), the mount of the detector can freely rotate around the centered normal axis of its top face (red arrow). The sample-detector distance can be increased (grey arrow) with extra spacer pieces.

Table 7. Angular and momentum resolution for 2 and 5 keV x-ray energy of the fixed and motorized in-vacuum detector assemblies.

Detector	$\Delta\delta$ (mrad)	$\Delta q_{2\text{keV}}$ (nm^{-1})	$\Delta q_{5\text{keV}}$ (nm^{-1})
Fixed	0.2–1.7	0.002–0.010	0.005–0.030
Motorized	0.3	0.002	0.006

3.1. Magnetic and orbital melting in Ca_2RuO_4

4d transition metal oxides exhibit interesting correlated states thanks to a strong spin–orbit coupling. At room temperature, a long-range orbital order in Ca_2RuO_4 forms a Mott insulator state, while an antiferromagnetic state is formed below a Néel temperature of 110 K. Both ordering phenomena can be observed by separate features in the resonant diffraction at the Ru L-II edge [80, 81]. The resonant (103) reflection from a (001)-cleaved crystal of Ca_2RuO_4 was investigated by the here described setup using the THz-compatible sample holder assembly and the fixed in-vacuum detector, in order to minimize x-ray signal absorption at the photon energies of just below 3 keV.

The sample was excited by near-IR pulses (800 nm) at an incidence angle of $\sim 10^\circ$. Laser excited and x-ray probed sample volumes were matched by using a grazing x-ray incidence angle of $< 3^\circ$. A $< 1 \text{ eV}$ bandwidth slice of the FEL spectrum was defined by the Bernina Si(111) double crystal monochromator. The x-ray photon energy dependent

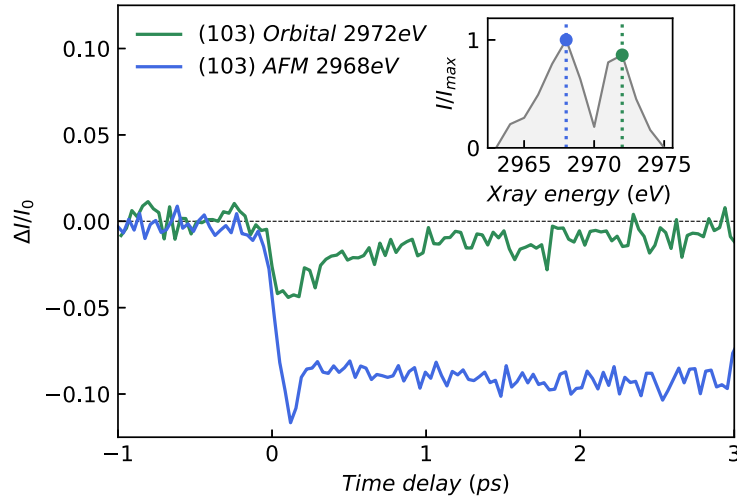


Figure 15. Relative change of the diffracted intensity of the (103) peak antiferromagnetic and orbital resonance at 2968 eV and 2972 eV following 800 nm excitation, respectively, measured at 20 K. The inset shows energy dependent peak intensities of the (103) reflection at the Ru *L*-II edge, revealing distinct features which represent orbital and magnetic orders [81].

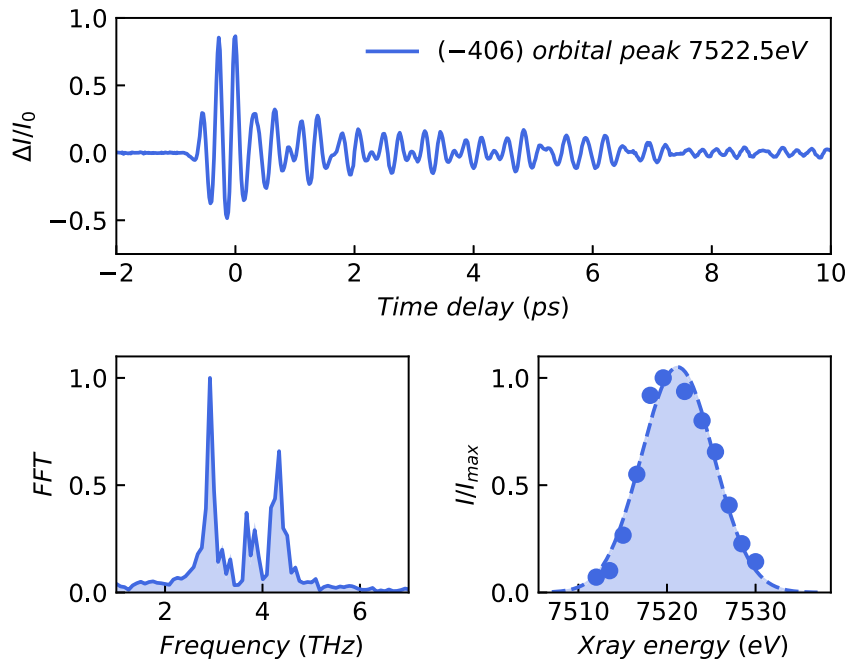


Figure 16. Relative change of the diffracted intensity of the (−406) orbital peak following THz excitation, measured at 5 K at the Tb *L*-edge at 7522.5 eV. The lower panels show the Fourier transform amplitude and a scan across the resonance of the Tb *L*-III edge.

integrated Bragg peak intensities could clearly resolve the previously reported resonant features of antiferromagnetic and orbital order, respectively at 2968 eV and 2972 eV (figure 15, inset). This was possible by suppressing the otherwise strong 3rd harmonic in the SASE beam by the monochromator and x-ray focusing mirrors, as well as minimized absorption of the tender x-ray fundamental through x-ray windows and air path. Transient pump/probe delay measurements of relatively high quality could be acquired at low temperature in the antiferromagnetic state of Ca_2RuO_4 . Their observed ultrafast dynamics differ at both energies (figure 15), implying a different response of magnetic and orbital order. These commissioning results already demonstrate that new information

on different material correlations can be obtained in the ultrafast time domain and thanks to the broad spectral range of brilliant FEL radiation.

3.2. Resonant excitation of a hybrid mode in $\text{Tb}_2\text{Ti}_2\text{O}_7$

The investigated material, $\text{Tb}_2\text{Ti}_2\text{O}_7$, is a magnetically frustrated Pyrochlore with no long-range magnetic order down to the lowest temperatures [82]. Characteristic for this rare earth titanate pyrochlore are degenerate ground states with very low energy crystal field excitations of the Tb 4f states at 1.5 meV (0.34 THz), 10 meV (2.4 THz) and 16 meV (3.8 THz) [83]. Neutron studies reported signatures of coupling between

acoustic phonon modes and these crystal field levels as the temperature is lowered enough for the crystal fields to become unoccupied [84]. Infrared-active absorption peaks were found to appear with the same temperature dependence in optical studies [85–87]. The goal of the commissioning experiment was to investigate the individual contribution of the structural and electronic degrees of freedom by resonantly exciting the mode and following selectively the structural and orbital order with (resonant) x-ray diffraction at SwissFEL.

The sample was cooled to 5 K to prevent thermal occupation of the crystal field states, and excited by single cycle broadband THz pulses with a frequency content of (0.3–4) THz (1–16) meV and a peak field of 1.12 MV cm^{-1} , as shown in figure 8.

The structural and orbital contributions were distinguished by tuning the photon energy of SwissFEL x-ray pulses on and off the Tb *L*-edge resonance at 7522.5 keV and measuring the time-resolved changes of structural and orbital diffraction peaks. Measurements of the resonant (–406) peak are shown in figure 16 for a sample temperature of 5 K. The time trace shows a large oscillatory response in the relative change in diffracted intensity $\Delta I/I_0$, exceeding 80%. The Fourier transform reveals oscillatory components at 2.9 THz, 3.7 THz and 4.3 THz, close to the third crystal field level. With the large observed signals, the experiment demonstrates not only the high sensitivity of materials to resonant excitation of low energy modes, it also shows the importance of selectively investigating the various degrees of freedom involved in coupled modes and the formation of material ground states. The results are still being analysed and will be published in a separate manuscript.

4. Conclusion

A compact vacuum chamber has been developed at the SwissFEL Bernina instrument that is dedicated for ultrafast resonant x-ray diffraction studies on correlated materials at cryogenic temperatures and optimized for selective low-energy excitations in the far infrared range. First successful commissioning experiments have demonstrated the capability of the setup to reach 5 K sample temperatures, perform resonant diffraction experiments in the tender to hard x-ray range, as well as provide THz pulses with field strengths exceeding 1 MV cm^{-1} . In particular, the design has proven technically robust and experiments with completely different parameters have been performed back-to-back without technical issues or hold ups. This is an important prerequisite for a large-scale user facility with very limited access to the setup prior to experiments.

Acknowledgments

This work was supported by the National Center of Competence in Research in Molecular Ultrafast Science and Technology (NCCR MUST—No. 51NF40-183615) from the Swiss National Science Foundations (SNSF). The THz chamber was funded by the SNSF R’Equip high-field THz source for pump–probe experiments at SwissFEL, Grant

No. 170760. MS was supported by the European Union’s Horizon 2020 research and innovation programme under the Marie Skłodowska Curie Grant Agreement No. 801459—FP-RESOMUS. We thank Marcel Locher, Achim Ammon, Renzo Rotundo and Andreas Keller for the detailed construction and technical guidance during the design process. Robert G Kälin and Alexander R Oggenfuss have been crucial for assembling the chamber and the experimental setup. We thank Seraphin Vetter and Aldo Mozzanica for fruitful discussions about the implementation of in-vacuum detector solutions. The authors thank Luc Patthey, Steven L Johnson and Gabriel Aeppli for their continuous support of the project.

Data availability statement

The data that support the findings of this study are available upon reasonable request from the authors.

ORCID iDs

Roman Mankowsky  <https://orcid.org/0000-0001-6784-0344>

Paul Beaud  <https://orcid.org/0000-0001-5028-9138>

Henrik Till Lemke  <https://orcid.org/0000-0003-1577-8643>

References

- [1] Dagotto E 1994 *Rev. Mod. Phys.* **66** 763–840
- [2] Imada M, Fujimori A and Tokura Y 1998 *Rev. Mod. Phys.* **70** 1039–263
- [3] Tokure Y 2000 *Science* **288** 462–8
- [4] Damascelli A, Hussain Z and Shen Z-X 2003 *Rev. Mod. Phys.* **75** 473–541
- [5] Keimer B, Kivelson S A, Norman M R, Uchida S and Zaanen J 2015 *Nature* **518** 179–86
- [6] Zeiger H J, Vidal J, Cheng T K, Ippen E P, Dresselhaus G and Dresselhaus M S 1992 *Phys. Rev. B* **45** 768–78
- [7] Merlin R 1997 *Solid State Commun.* **102** 207–20
- [8] Yusupov R, Mertelj T, Kabanov V V, Brazovskii S, Kusar P, Chu J-H, Fisher I R and Mihailovic D 2010 *Nat. Phys.* **6** 681–4
- [9] Stevens C J, Smith D, Chen C, Ryan J F, Podobnik B, Mihailovic D, Wagner G A and Evetts J E 1997 *Phys. Rev. Lett.* **78** 2212–5
- [10] Averitt R D and Taylor A J 2002 *J. Phys.: Condens. Matter* **14** R1357–90
- [11] Demsar J, Podobnik B, Kabanov V V, Wolf T and Mihailovic D 1999 *Phys. Rev. Lett.* **82** 4918–21
- [12] Fiebig M, Miyano K, Tomioka Y and Tokura Y 2000 *Appl. Phys. B* **71** 211–5
- [13] Cavalleri A, Dekorsy T, Chong H H W, Kieffer J C and Schoenlein R W 2004 *Phys. Rev. B* **70** 161102
- [14] Kübler C, Ehrke H, Huber R, Lopez R, Halabica A, Haglund R F and Leitenstorfer A 2007 *Phys. Rev. Lett.* **99** 116401
- [15] Mankowsky R, von Hoegen A, Först M and Cavalleri A 2017 *Phys. Rev. Lett.* **118** 197601
- [16] Perfetti L, Loukakos P A, Lisowski M, Bovensiepen U, Berger H, Biermann S, Cornaglia P S, Georges A and Wolf M 2006 *Phys. Rev. Lett.* **97** 067402
- [17] Schmitt F *et al* 2008 *Science* **321** 1649
- [18] Rohwer T *et al* 2011 *Nature* **471** 490–3

- [19] Siwick B J, Dwyer J R, Jordan R E and Miller R J D 2003 *Science* **302** 1382–5
- [20] Gedik N, Yang D-S, Logvenov G, Bozovic I and Zewail A H 2007 *Science* **316** 425
- [21] Eichberger M, Schäfer H, Krumova M, Beyer M, Demsar J, Berger H, Moriena G, Sciaini G and Miller R J D 2010 *Nature* **468** 799–802
- [22] Mannebach E M et al 2015 *Nano Lett.* **15** 6889–95
- [23] Rousse A, Rischel C and Gauthier J-C 2001 *Rev. Mod. Phys.* **73** 17–31
- [24] Rose-Petruck C et al 1999 *Nature* **398** 310–2
- [25] Lindenberg A M et al 2000 *Phys. Rev. Lett.* **84** 111–4
- [26] Cavalleri A, Tóth C, Siders C W, Squier J A, Ráksi F, Forget P and Kieffer J C 2001 *Phys. Rev. Lett.* **87** 237401
- [27] Reis D A et al 2001 *Phys. Rev. Lett.* **86** 3072–5
- [28] Cavalleri A, Wall S, Simpson C, Stutz E, Ward D W, Nelson K A, Rini M and Schoenlein R W 2006 *Nature* **442** 664–6
- [29] Bargheer M, Zhavoronkov N, Gritsai Y, Woo J C, Kim D S, Woerner M and Elsaesser T 2004 *Science* **306** 1771–3
- [30] Johnson S L, Beaud P, Vorobeva E, Milne C J, Murray É D, Fahy S and Ingold G 2009 *Phys. Rev. Lett.* **102** 175503
- [31] Beaud P, Johnson S L, Vorobeva E, Staub U, Souza R A D, Milne C J, Jia Q X and Ingold G 2009 *Phys. Rev. Lett.* **103** 155702
- [32] Zhou S Y et al 2014 *Sci. Rep.* **4** 4050
- [33] Laulhé C et al 2017 *Phys. Rev. Lett.* **118** 247401
- [34] Emma P et al 2010 *Nat. Photon.* **4** 641–7
- [35] Ishikawa T 2012 *Nat. Photon.* **6** 540–4
- [36] Kang H-S et al 2017 *Nat. Photon.* **11** 708–13
- [37] Decking W et al 2020 *Nat. Photon.* **14** 391–7
- [38] Prat E et al 2020 *Nat. Photon.* **14** 748+
- [39] Mankowsky R et al 2014 *Nature* **516** 71–3
- [40] Gerber S et al 2017 *Science* **357** 71–5
- [41] Clark J N et al 2013 *Science* **341** 56–9
- [42] Singer A et al 2016 *Phys. Rev. Lett.* **117** 056401
- [43] Langner M C et al 2017 *Phys. Rev. Lett.* **119** 107204
- [44] Singer A et al 2018 *Phys. Rev. Lett.* **120** 207601
- [45] Dornes C et al 2019 *Nature* **565** 209–12
- [46] Kozina M et al 2019 *Nat. Phys.* **15** 387–92
- [47] Vidal F et al 2019 *Phys. Rev. Lett.* **122** 145702
- [48] Lindenberg A M, Johnson S L and Reis D A 2017 *Annu. Rev. Mater. Res.* **47** 425–49
- [49] Buzzi M, Först M, Mankowsky R and Cavalleri A 2018 *Nat. Rev. Mater.* **3** 299–311
- [50] Chuang Y D et al 2013 *Phys. Rev. Lett.* **110** 127404
- [51] Johnson S L et al 2012 *Phys. Rev. Lett.* **108** 037203
- [52] de Jong S et al 2013 *Nat. Mater.* **12** 882–6
- [53] Beaud P et al 2014 *Nat. Mater.* **13** 923–7
- [54] Kubacka T et al 2014 *Science* **343** 1333–6
- [55] Ament L J P, van Veenendaal M, Devereaux T P, Hill J P and van den Brink J 2011 *Rev. Mod. Phys.* **83** 705–67
- [56] Parchenko S et al 2020 *Phys. Rev. Res.* **2** 023110
- [57] Trigo M et al 2013 *Nat. Phys.* **9** 790–4
- [58] Guzelturk B et al 2021 *Nat. Mater.* **20** 618–23
- [59] Wall S et al 2018 *Science* **362** 572–6
- [60] Kampfrath T, Tanaka K and Nelson K A 2013 *Nat. Photon.* **7** 680–90
- [61] Först M, Manzoni C, Kaiser S, Tomioka Y, Tokura Y, Merlin R and Cavalleri A 2011 *Nat. Phys.* **7** 854–6
- [62] Hu W et al 2014 *Nat. Mater.* **13** 705–11
- [63] Baierl S, Hohenleutner M, Kampfrath T, Zvezdin A K, Kimel A V, Huber R and Mikhaylovskiy R V 2016 *Nat. Photon.* **10** 715+
- [64] Nemec P, Fiebig M, Kampfrath T and Kimel A V 2018 *Nat. Phys.* **14** 229–41
- [65] Rini M, Tobey R a, Dean N, Itatani J, Tomioka Y, Tokura Y, Schoenlein R W and Cavalleri A 2007 *Nature* **449** 72–4
- [66] Liu M et al 2012 *Nature* **487** 345–8
- [67] Esposito V et al 2017 *Phys. Rev. Lett.* **118** 247601
- [68] Doering D et al 2011 *Rev. Sci. Instrum.* **82**
- [69] Galler A et al 2019 *J. Synchrotron Radiat.* **26** 1432–47
- [70] Ingold G et al 2019 *J. Synchrotron Radiat.* **26** 874–86
- [71] You H 1999 *J. Appl. Crystallogr.* **32** 614–23
- [72] Wu Q and Zhang X C 1995 *Appl. Phys. Lett.* **67** 3523
- [73] Casalbuoni S, Schlarb H, Schmidt B, Schmüser P, Steffen B and Winter A 2008 *Phys. Rev. ST Accel. Beams* **11** 072802
- [74] Brunner F D J, Johnson J A, Grübel S, Ferrer A, Johnson S L and Feurer T 2014 *J. Opt. Soc. Am. B* **31** 904–10
- [75] Leitenstorfer A, Hunsche S, Shah J, Nuss M C and Knox W H 1999 *Appl. Phys. Lett.* **74** 1516–8
- [76] Berozashvili Y, Machavariani S, Natsvlishvili A and Chirakadze A 1989 *J. Phys. D: Appl. Phys.* **22** 682–6
- [77] Bakker H J, Cho G C, Kurz H, Wu Q and Zhang X-C 1998 *J. Opt. Soc. Am. B* **15** 1795–801
- [78] Lerch P et al 2012 *J. Phys.: Conf. Ser.* **359** 012003
- [79] Mozzanica A et al 2018 *Synchrotron Radiat. News* **31** 16–20
- [80] Zegkinoglou I et al 2005 *Phys. Rev. Lett.* **95** 136401
- [81] Pincini D, Veiga L S I, Dashwood C D, Forte F, Cuoco M, Perry R S, Bencok P, Boothroyd A T and McMorro D F 2019 *Phys. Rev. B* **99** 075125
- [82] Hirschberger M, Krizan J W, Cava R J and Ong N P 2015 *Science* **348** 106–9
- [83] Ruminy M, Pomjakushina E, Iida K, Kamazawa K, Adroja D T, Stühr U and Fennell T 2016 *Phys. Rev. B* **94** 024430
- [84] Fennell T et al 2014 *Phys. Rev. Lett.* **112** 017203
- [85] Lummen T T A, Handayani I P, Donker M C, Fausti D, Dhalenne G, Berthet P, Revcolevschi A and van Loosdrecht P H M 2008 *Phys. Rev. B* **77** 214310
- [86] Constable E et al 2017 *Phys. Rev. B* **95** 020415
- [87] Amelin K et al 2020 *Phys. Rev. B* **102** 134428